Academic Journal of Science and Technology,
October, 2024, vol.4, No.1, p205-213

Synthesis and Characterization of Cobalt and Copper Nanoparticles by Amino Acid.

Abdussallam N. Eldewik[1], Huda. M. Al-Ashkham[1*].

1. Department of Chemistry, The Libyan Academy for Postgraduate Studies

ABSTRACT

A quantitative study of the synthesis and characterization of copper oxide, cobalt oxide nanoparticles and their mixtures has been considered. With special emphasis on the hydrothermal synthesis in organic media of glutamic acid.

The aim of the work is to initiate a new line of research on the synthesis and characterization of these particles and is to develop high-quality nanoparticles for use in more important applications. It has been characterized using several techniques such as Fourier Transform Infrared spectroscopy (FT-IR), Energy Dispersive X-ray EDX, Scanning Electron Microscopy (SEM), X-ray diffraction (XRD), Thermogravimetric analysis (TGA), and Diffuse reflectance UV-Vis analysis.

The results of these devices indicated the formation of copper oxide nanoparticles with highly purified crystalline nanostructures, as well as very minimal incorporation of cobalt into the formulation. Thermal gravimetric analysis (TGA) confirmed their thermal stability, while ultraviolet radiation (UV-Vis) showed that some samples are insulators and others are semiconductors.

KEYWORDS: *Hydrothermal synthesis, Copper(I) oxide NPs, Cobalt oxide NPs.*

* *Corresponding author:* lion4040400@gmail.com

INTRODUCTION

Copper and cobalt nanoparticles are produced, with emphasis on these metals, as the transition metals of cobalt and copper have numerous uses in lithium-ion batteries, gas sensing, data storage, and catalysis. The strong conductivity of copper nanoparticles distinguishes them from other metal nanoparticles (Yuanchun et al., 2008). Amino acid (glutamic acid) is a bio-based and environmentally friendly polymer material with water solubility and strong biocompatibility. It has many uses in medicine, food, cosmetics, and other fields (Liu, Z et al., 2023). They used the thermal process because it is very popular among many industrial technologies because it is easy to use, inexpensive, and versatile. The heterogeneity of a closed system operating at room temperature and atmospheric pressure in the presence of aqueous or non-aqueous solvents prevents the vapor pressure of the substance and allows it to build up, stopping the decomposition of certain molecules at high temperatures and reducing the possibility of generating oxide materials by a given thermal process and regulate atmospheric conditions, generating crystals of consistent and acceptable quality (Tavakoli et al., 2007).

Typically, metal nanoparticles are formed on mono- or bi-metallic structures. One type of metal with unique chemical and physical properties forms monometallic nanoparticles. Because of their distinct optical, electrical, magnetic, and catalytic properties which, for the most part, distinguish them from their monometallic counterparts. Bimetallic nanoparticles (NPs) have attracted much attention in the past 10 years from both scientists and researchers. Bimetallic nanoparticles (NPs) can have a wide range of shapes and structures and are created by mixing two distinct types of metal nanoparticles. Due to the synergistic qualities between the two distinct metal moieties, they usually display more interesting properties (Arora et al., 2020).

When compared to similar monometallic NPs, properties and performance can be optimized by choosing the right metal combination and support and by optimizing the composition of each type of metal.

Combining two distinct metals in a reaction vessel under ideal conditions produces a variety of structural and morphological changes, which are used to create metallic nanoparticles. A variety of bimetallic particles can be produced by mixing different metals, including noble metals and transition metals (Idris & Roy, 2023).

MATERIALS AND METHODS

Samples of copper and cobalt and their mixtures at different concentrations were prepared by the same thermal method. (Cu100%). (Cu 83.3%, Co 16.7%), (Cu 66.7%, Co 33.3%), (Co 50%, Cu 50%), (Cu 16.7%, Co 83.3%). 10 mL of DMF was added to each sample by pipette under magnetic stirring at room temperature. The solution was stirred intensively for 1 hour, the pH of the resulting solution was measured, and the results are listed in Table 1. It was transferred to a stainless-steel autoclave with a Teflon liner and heated at 120 °C for 24 hours in an oven for all samples. After that, It was left to cool at room temperature, then the sediment was rinsed with distilled water several times to remove any impurities and filtered, and the color of the sediment XRD spectra were as shown in Figure 1. The weight of the sediment was measured using a sensitive balance, and the weights are shown in Table 1. The first experiment was repeated with the same steps but remained in the oven for 48 hours, and all its results were completely consistent with the sample that remained for 24 hours.

Table 1: Weights and pH values for the product samples:

sample	concentration	pH	weight	Heating Time
1-A	(Cu 100%)	2.22	0.768g	48h
1-B	(Cu 100%)	2.28	0.5g	24h
2	(Cu83.3%, Co 16.7%)	2.37	0.5g	24h
3	(Co 50%, Cu 50%)	3.62	0.406g	24h
4	(Cu66.7%, Co 33.3%)	3.56	0.7g	24h
5	(Cu16.7%, Co 83.3%)	2.67	0.1g	24h

RESULTS AND DISCUSSION:

XRD ANALYSIS:

Figure 1 displays the powder XRD pattern of the product samples. The diffraction peaks are at 2θ, which are 29.53°, 36.39°, 42.24°, 61.27°, and 77.39° in the sample. The results shown here are consistent with values found in the literature (JCPDS reference code: 1531-075-01). The samples match previously published research (Laidoudi et al., 2013), (Kooti, 2010), which indicates the formation of a pure Cu2O cubic phase Face-centered cubic (FCC). From the XRD data, the crystallite size was calculated according to the Schreyer equation and the values are shown in Table 2.

$D= 0.9\lambda/(\beta.\cos\theta)$

Where 'λ' is the wave length of X-ray (0.1541 nm), 'β' is full width at half maximum (FWHM), 'θ' is the diffraction angle, and 'D' is particle diameter size (Theivasanthi & Alagar, 2010). In the second sample, it was noted that the peaks appear at 42.28° and 52.46°, and it is indicated that it can be considered cubic cobalt oxide according to (ICDD 00-015-0806). Likewise, the 2θ values in the rest of the samples show the appearance of Cu2O and CoO.

The lattice modulus value of the copper phase did not vary significantly across samples. It was about unit cell in the first sample (a = 4.27 Å). We note that in the second and fourth samples it was (a = 4.94 Å) and in the third and fifth samples (a = 4.96 Å) with a slight change in the crystal lattice constant, which indicates little entry of cobalt, and this is very important, which strongly indicates the formation of bimetallic NPs. This small change is because the change in the lattice constant will be small when the new atom is of a similar size to the existing atoms, resulting in a small change in the crystal lattice constant. It was calculated from the Bragg equation

The presence of both crystals in mixtures containing copper and cobalt is not new, as these crystalline elements are known to be immiscible under ambient conditions, according to (Subramanian et al., 2009).

Some studies indicate that cobalt atoms cannot be replaced by copper, which is consistent with the results of (Eugénio et al., 2016). The use of a Co Kα radiation source can have the effect of providing better resolution in cobalt diffraction patterns, since Cu Kα radiation often leads to higher fluorescence and therefore more background noise in the XRD spectra of cobalt nanoparticles (Saw, 2005).

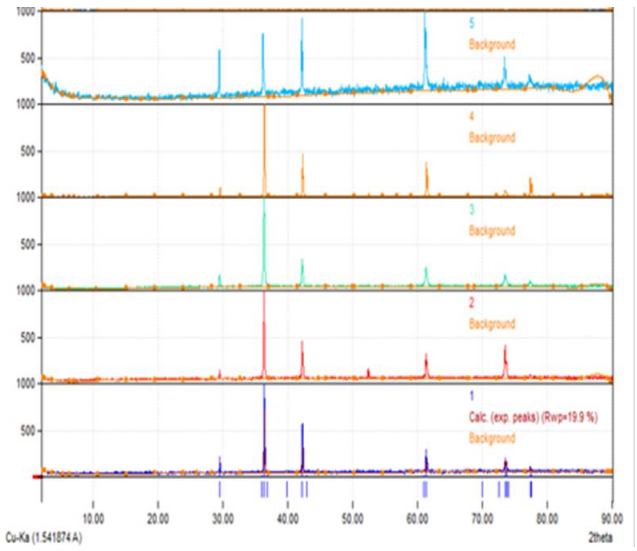

Figure 1 Powder XRD pattern of samples 1. (Cu2O). 2. (Cu 1.96Co0.04 O).3. (Cu1.99 Co0.01 O).4. (Cu 1.98Co0.02 O).5. (Cu1.99 Co0.04 O)

Table2: Values of 2Θ for Cu2O, CoO XRD spectra and crystal Samples size:

Experimental XRD angle [2θ]	Standard XRD angle [2θ]		Samples size	
29.52°	29.60°	Cu_2O	Sample1	1.23nm
36.39°	36.45°	Cu_2O	Sample2	1.26nm
42.23°	42.34°	Cu_2O	Sample3	1.82nm
61.27°	61.40°	Cu_2O	Sample4	1.47nm
77.38°	77.61°	Cu_2O	Sample5	1.01nm
52.46°	51.5°	CoO		
43.28°	44.3°	CoO		

EDX AND SEM ANALYSIS:

These samples were covered with a thin layer of gold to enhance the emission of secondary electrons and provide a homogeneous surface for analysis and imaging. As did Leslie and Mitchell (2007). In Figure 2, SEM images of sample 1 are shown. The sample appears to contain uniformly octagonal nanoparticles(Leslie & Mitchell, 2007). They were confirmed by energy dispersive X-ray (EDX) analysis, quantification and stoichiometry of Cu2O NPs showed that there was a uniform distribution of copper to oxygen (atomic ratio 2:1) in Cu2O NPs in the first sample that did not contain cobalt, as shown in Table 3.

In the model of Figure 2 and SEM images, these phenomena are mainly due to the conversion of parts of Cu2O into copper particles under the action of the strong reducing agent carbon The presence on the roof.; the holes in the faces grow a lot, and the structure of some octahedrons is damaged. These phenomena are mainly caused by the conversion of parts of Cu2O into Cu particles under the action of a strong reducing agent, which is consistent with the literature (Zhu et al., 2013). They were confirmed by EDX analysis. . In the remaining samples, EDX values show that cobalt has a very weak entry effect, as shown in the table3. The SEM images in Figure 2, confirm that they are pure single crystals of copper oxide nanoparticles.

Table3: Chemical composition of the resulted samples of EDX.

sample	**O**	**Cu**	**Co**
1	**1**	**2**	**0**
2	**1**	**1.96**	**0.04**
3	**1**	**1.99**	**0.01**
4	**1**	**1.98**	**0.015**
5	**1**	**1.99**	**0.01**

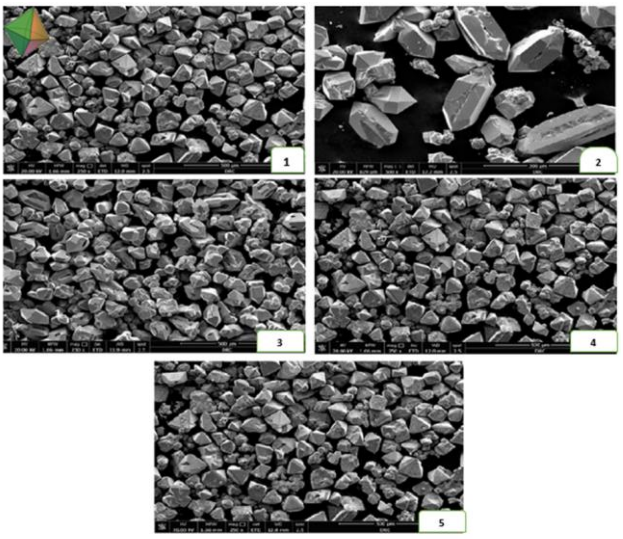

Figure 2 SEM pattern of samples 1. (Cu2O). 2. (Cu 1.96Co0.04 O).3. (Cu1.99 Co0.01 O).4. (Cu 1.98Co0.02 O).5. (Cu1.99 Co0.04 O).

FT-IR ANALYSIS:

The IR pattern supporting Cu_2O demonstrates the pure crystalline nature of the metal oxide, and the sample variations in the IR spectra shown in Figure 3 are consistent with previously published research (Ahmed et al., 2011),(Le et al., 2021). Frequency bands below 500cm^{-1} can also be assigned to Cu-O bonds in Cu_2O phases in all spectra, as well as at 665cm^{-1} which are vibrations for the Co-O (Birhi et al., 2023). The presence of narrow and broad bands in the spectrum can be explained by the presence of crystalline lines and amorphous nanostructures on the surface of the nanoparticles. The establishment of chemical interactions between copper and oxygen atoms on the surface of copper nanoparticles was demonstrated by infrared spectroscopy examinations performed at frequencies of 500cm^{-1}. They provide details of the oxidation reactions that occur on the surface of nanoparticles (Markova, 2010).

The FT-IR spectrum of samples containing Cu_2O is compared with that of pure GLU. The bands resulting from OH stretching and CH stretching in the regions 3000-3700 and 2800-3000cm^{-1} change significantly because they completely disappear from the copper oxide spectrum. The region 700–1700 cm^{-1} and the intensity of the band at 630 cm^{-1} were similarly affected, where the Cu-O group greatly enhanced the CH_2 vibration.

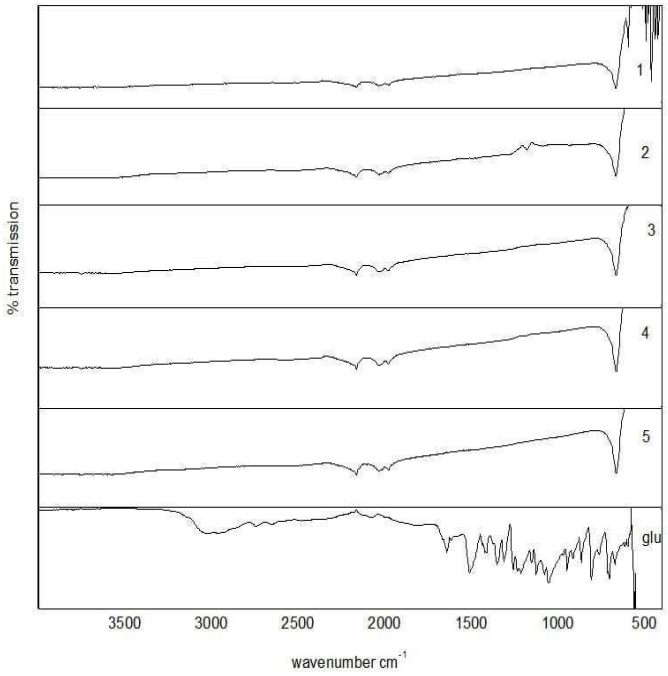

Figure 3 FT-IR pattern of the resulted samples and number 6 of pure glutamic acid,1. (Cu2O). 2. (Cu 1.96Co0.04 O).3. (Cu1.99 Co0.01 O).4. (Cu 1.98Co0.02 O).5. (Cu1.99 Co0.04 O).

UV-VIS DIFFUSE REFLECTANCE ANALYSIS:

The UV diffuse reflectance spectrum was analyzed to extract the band gap. The idea arises from the Kubilka-Munk theory (R), which describes the behavior of light traveling inside a light-scattering sample. The energy difference between the top of the valence band and the bottom of the conduction band, which is where electrons can go from the valence band to the conduction band, is referred to as the "band gap". An electron needs a certain minimum of energy to make the passage from the valence band to the conduction band. Plotting the square product of the absorption coefficient and energy $(\alpha E)2$ against energy E ($(\alpha E)2$ vs. E) yields the band gap. The band gap can be obtained by extending

the straight line from the straight part of the graph as shown in figure 4, that touches the E axis, where E = hv, h Planck constant, and v frequency (Abdullahi et al., 2016). The optical band gap has also been determined experimentally and also by theoretical modeling by different research groups; it falls in the range (2.0–2.5eV) for Cu2O. (Gupta et al., 2018), The band gaps of nano-Cu2O (2.15eV) and (2.25eV) were reported by (Muthukumaran et al., 2019),(Ma et al., 2010) respectively. Though it is not unusual for band gap to change with nano-size and structure, our results for the range gap as shown in the table 4 were much higher than theirs. Grain size is one of the factors that causes large variation in the stated value of the band gap. Due to quantum confinement effects, the band gap value increases as the size of the CuO nanoparticles decreases. It was observed that this value changed from 3.72eV to 4.02eV when the particle size decreased from 20nm to 11nm. This is what Fishman et al (Fishman et al.,2016), It is also consistent with Mahajan's et al.'s results. When the particle Cu2O size decreases, the value increases for the band gap (Mahajan, M. B. et al., 2009). After calculating the band gap for all samples, the values were varies, and this is attributed to the variation of the conductivity of the materials, according to (Dharma, 2009).

Table 4: Band Gap Values of resulted sample:

Samples	Band Gap Value	(>3 = insulator) (<3 = semiconductor)
1	1.70 ev	semiconductor
2	3.51 ev	Insulator
3	2.50 ev	Semiconductor
4	3.07 ev	Insulator
5	3.50 ev	Insulator

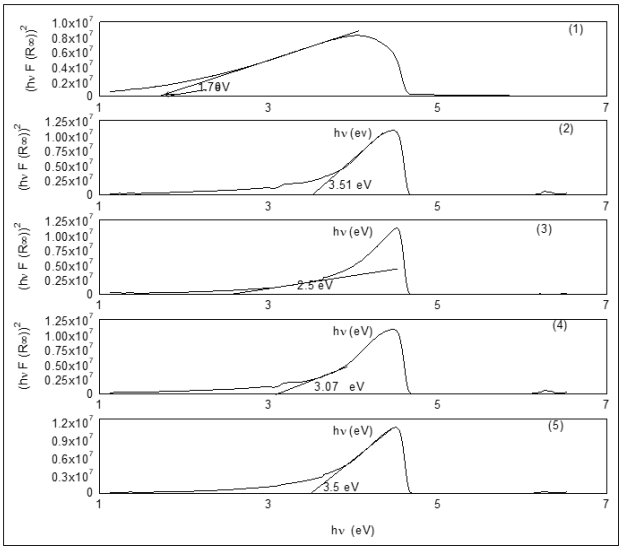

Figure 4: UV-Vis diffuse reflectance pattern of resulted samples 1. (Cu_2O). 2. ($Cu_{1.96}Co_{0.04}O$).3. ($Cu_{1.99}Co_{0.01}O$).4. ($Cu_{1.98}Co_{0.02}O$).5. ($Cu_{1.99}Co_{0.04}O$).

TGA ANALYSIS:

Thermal gravimetric analysis (TGA) and differential thermal analysis (DTG) were used to measure the thermal analysis in the range up to 700°C for the samples as shown in Figure 5. first sample, the initial weight loss of approximately 5.21% by weight is due to the evaporation of water at the surface at 180°C. It is an endothermic reaction, and at a temperature of 200°C, according to (Weiss et al., 2018), the decomposition of organic materials adsorbed on

the surface of the samples begins, especially glutamate, which is an endothermic reaction.

We notice a sudden increase in the rate after 400°C, and almost similar results appeared regarding this increase, and they explained it by the appearance of oxygen and its spread on the surface, leaving empty pore spaces to gradually gather to form larger pores. This results in a temporary weight gain, which spreads according to the Kirkendall effect (Gao et al., 2015). Gainsford believed that the oxide cracked or crystallized to form a porous material. Many minerals show changes in reaction rate at different temperature points (Gaisford et al., 2016).

No further significant weight loss was observed, thereby supporting the formation of crystallinity with high purity and indicating that the synthesized Cu_2O-NPs exhibited excellent thermal stability (TGA) for these samples is very similar in weight loss at around 320°C. The percentage of the sample 2 was 0.78%, as shown in Figure 5, while the percentage of the sample 5 was 0.62%, as shown in Figure 5. This is a very small loss, almost negligible, and this indicates the high thermal stability of these samples. We also notice an increase in weight above 340 degrees Celsius, which was explained previously.

As for the third sample, it lost about 6.72% of its weight at a temperature of 380 degrees Celsius. 0.7% of it at 150°C. This is due to the evaporation of water from the surface, which is an endothermic reaction. The remaining 6% is the result of the decomposition of organic materials adsorbed on the surface, which is also an endothermic reaction behavior.

In sample 4, it lost about 15.28% of its weight at a temperature of 380°C. 1% of it at 150°C. This results from water evaporating off the surface.

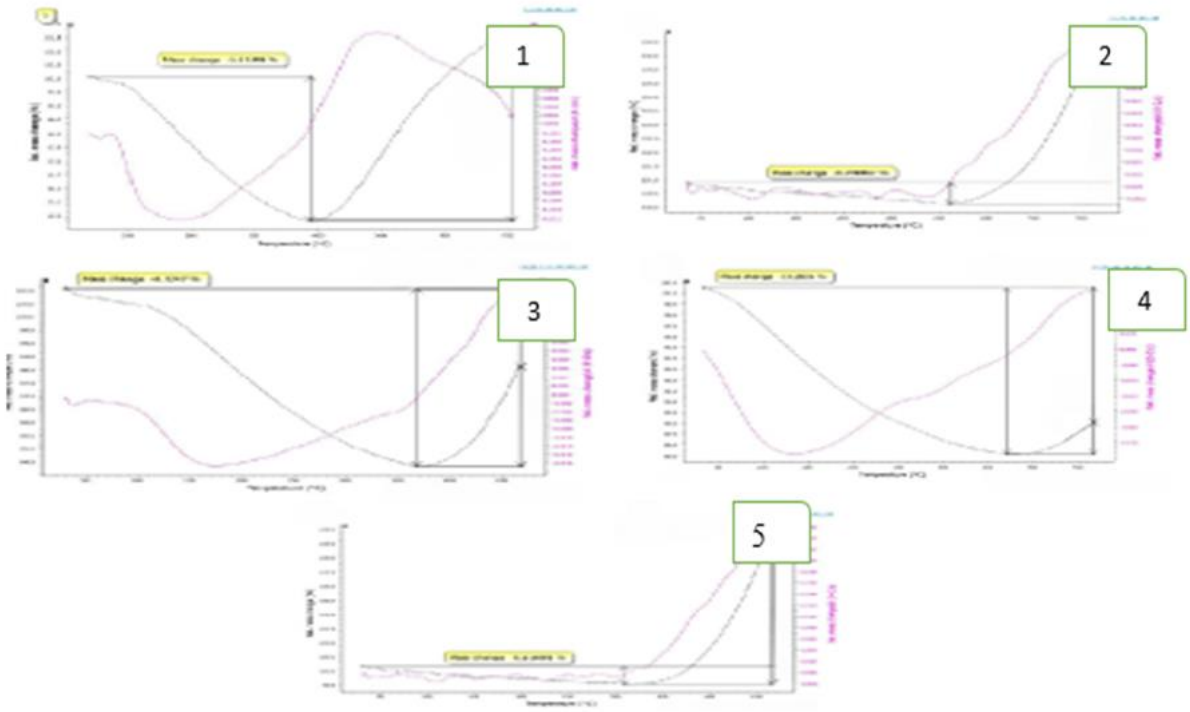

Figure *5* TGA pattern of samples, 1. (Cu_2O). 2. ($Cu_{1.96}Co_{0.04}O$).3. ($Cu_{1.99}Co_{0.01}O$).4. ($Cu_{1.98}Co_{0.02}O$).5. ($Cu_{1.99}Co_{0.04}O$).

CONCLUSION:

Black and violet nanocobalt and copper oxides were inexpensively synthesized and characterized using UV-visible spectrophotometry, Fourier transform infrared spectroscopy, and scanning electron microscopy. The synthesized nanoparticles also showed high crystallinity, and good XRD results indicate the formation of pure Cu_2O cubic phase (FCC). From the XRD data, the average crystalline size of the samples was calculated and was 1.820nm. The sample appears to contain uniformly shaped octagonal nanoparticles. This was confirmed by quantum energy dispersive X-ray (EDX) analysis and stoichiometry of the Cu_2O NPs, which showed that there was a uniform distribution of copper to oxygen (atomic ratio 2:1) in the Cu_2O NPs in the first sample that did not contain cobalt. Samples with a small change in the crystal lattice constant indicate very little cobalt ingress.

Likewise in FT-IR, frequency bands below 500 cm^{-1} for Cu-O bonds in Cu_2O phases appear in all spectra, as well as at 665 cm^{-1}, which are vibrations of Co-O, As the size and structure of the nanoscale changed, our band gap results were much higher than theirs. Grain size is one of the factors that causes large variation in the stated value of the band gap. When the Cu_2O particle size decreases, the band gap value increases. After calculating the band gap for all samples, the values varied, and this is due to the different conductivity of the

materials. Some were insulators, and others were semiconductors, allowing them to be used in many applications. The TGA results were thermally stable. We notice a sudden increase in the rate after 400°C, and almost similar results appeared regarding this increase, and they explained it by the appearance of oxygen and its spread on the surface, leaving empty pore spaces to gradually gather to form larger pores.no further significant weight loss was observed, thereby supporting the formation of crystallinity with high purity and indicating that the synthesized Cu_2O-NPs exhibited excellent thermal stability (TGA).

REFERENCES:

1. Abdullahi, S. S., Güner, S., Musa, Y. K. I. M., Adamu, B. I., & Abdulhamid, M. I. (2016). Sımple method for the determınatıon of band gap of a nanopowdered sample usıng Kubelka Munk theory. *NAMP J*, *35*, 241-246.
2. Ahmed, A., Gajbhiye, N. S., & Joshi, A. G. (2011). Low cost, surfactant-less, one pot synthesis of Cu2O nano-octahedra at room temperature. *Journal of Solid State Chemistry*, *184*(8), 2209-2214.
3. Arora, N., Thangavelu, K., & Karanikolos, G. N. (2020). Bimetallic nanoparticles for antimicrobial applications. *Frontiers in Chemistry*, *8*, 412.
4. Birhi, D. N., Iftitah, E. D., & Warsito, W. (2023). Use of CoO/ZnAl2O4 Catalysts and Microwaved Assisted in Vanillin Synthesis. *Jurnal Kimia Valensi*, *9*(1), 76-88.
5. Dharma, J., Pisal, A., & Shelton, C. T. (2009). Simple method of measuring the band gap energy value of TiO2 in the powder form using a UV/Vis/NIR spectrometer. *Application Note Shelton, CT: PerkinElmer*, 1-4.
6. Eugénio, S., Demirci, U. B., Silva, T. M., Carmezim, M. J., & Montemor, M. F. (2016). Copper-cobalt foams as active and stable catalysts for hydrogen release by hydrolysis of sodium borohydride. *international journal of hydrogen energy*, *41*(20), 8438-8448.
7. Fishman, Z. S., Rudshteyn, B., He, Y., Liu, B., Chaudhuri, S., Askerka, M., ... & Pfefferle, L. D. (2016). Fundamental role of oxygen stoichiometry in controlling the band gap and reactivity of cupric oxide nanosheets. *Journal of the American Chemical Society*, *138*(34), 10978-10985.
8. Gaisford, S., Kett, V., & Haines, P. (Eds.). (2016). *Principles of thermal analysis and calorimetry*. The Royal Society of Chemistry.
9. Gao, L., Pang, C., He, D., Shen, L., Gupta, A., & Bao, N. (2015). Synthesis of hierarchical nanoporous microstructures via the Kirkendall effect in chemical reduction process. *Scientific reports*, *5*(1), 16061.
10. Gupta, D., Meher, S. R., Illyaskutty, N., & Alex, Z. C. (2018). Facile synthesis of Cu2O and CuO nanoparticles and study of their structural, optical and electronic properties. *Journal of Alloys and Compounds*, *743*, 737-745.
11. Idris, D. S., & Roy, A. (2023). Synthesis of bimetallic nanoparticles and applications—an updated review. *Crystals*, *13*(4), 637.
12. Kooti, M., & Matouri, L. (2010). Fabrication of nanosized cuprous oxide using fehling's solution. *Scientia Iranica*, *17*(1).
13. Laidoudi, S., Bioud, A. Y., Azizi, A., Schmerber, G., Bartringer, J., Barre, S., & Dinia, A. (2013). Growth and characterization of electrodeposited Cu2O thin films. *Semiconductor science and technology*, *28*(11), 115005.
14. Le, G. N. T., Cong, T. N., Van, T. P., Tuyet, M. N. T., Thi, L. N., Dang, C. H., ... & Lan, A. L. T. (2021). Green synthesis of cuprous oxide (Cu2O) nano particles using aloe vera plant. *Vietnam Journal of Catalysis and Adsorption*, *10*(2), 54-58.

15. Leslie, S. A., & Mitchell, J. C. (2007). Removing gold coating from SEM samples. *palaeontology*, *50*(6), 1459-1461.
16. Liu, Z., He, Y., & Ma, X. (2023). Preparation, Characterization and Drug Delivery Research of γ-Polyglutamic Acid Nanoparticles: A Review. *Current Drug Delivery*.
17. Ma, L. L., Li, J. L., Sun, H. Z., Qiu, M. Q., Wang, J. B., Chen, J. Y., & Yu, Y. (2010). Self-assembled Cu2O flowerlike architecture: polyol synthesis, photocatalytic activity and stability under simulated solar light. *Materials Research Bulletin*, *45*(8), 961-968.
18. Mahajan, M. B., Pavan, M. S., & Joy, P. A. (2009). Ferromagnetic properties of glucose coated Cu2O nanoparticles. *Solid state communications*, *149*(47-48), 2199-2201.
19. Markova-Deneva, I. (2010). Infrared spectroscopy investigation of metallic nanoparticles based on copper, cobalt, and nickel synthesized through borohydride reduction method. *Journal of the University of Chemical Technology and Metallurgy*, *45*(4), 351-378.
20. Muthukumaran, M., Niranjani, S., Barnabas, K. S., Narayanan, V., Raju, T., & Venkatachalam, K. (2019). Green route synthesis and characterization of cuprous oxide (Cu2O): Visible light irradiation photocatalytic activity of MB dye. Materials Today: Proceedings, 14, 563-568.
21. Saw, C. K. (2005). X-Ray Scattering Techniques for Characterization of Nanosystems in Lifescience. Nanotechnologies for Life Sciences, 3(UCRL-JRNL-211387).
22. Subramanian, N. D., Balaji, G., Kumar, C. S., & Spivey, J. J. (2009). Development of cobalt–copper nanoparticles as catalysts for higher alcohol synthesis from syngas. Catalysis Today, 147(2), 100-106.
23. Tavakoli, A., Sohrabi, M., & Kargari, A. (2007). A review of methods for synthesis of nanostructured metals with emphasis on iron compounds. chemical papers, 61(3), 151-170.
24. Theivasanthi, T., & Alagar, M. (2010). X-ray diffraction studies of copper nanopowder. arXiv preprint arXiv:1003.6068.
25. Weiss, I. M., Muth, C., Drumm, R., & Kirchner, H. O. (2018). Thermal decomposition of the amino acids glycine, cysteine, aspartic acid, asparagine, glutamic acid, glutamine, arginine and histidine. BMC biophysics, 11(1), 1-15.
26. Yuanchun, Q., Yanbao, Z., & Zhishen, W. (2008). Preparation of cobalt oxide nanoparticles and cobalt powders by solvothermal process and their characterization. Materials Chemistry and Physics, 110(2-3), 457-462.
27. Zhu, H., Du, M., Yu, D., Wang, Y., Wang, L., Zou, M., ... & Fu, Y. (2013). A new strategy for the surface-free-energy-distribution induced selective growth and controlled formation of Cu 2 O–Au hierarchical heterostructures with a series of morphological evolutions. Journal of Materials Chemistry A, 1(3), 919-929.